PAPER

Gyrokinetic simulations of toroidal Alfvén eigenmodes excited by energetic ions and external antennas on the Joint European Torus

IOP Publishing | International Atomic Energy Agency Nuclear Fusion

Nucl. Fusion **59** (2019) 026008 (10pp) https://doi.org/10.1088/1741-4326/aaf430

Gyrokinetic simulations of toroidal Alfvén eigenmodes excited by energetic ions and external antennas on the Joint European Torus

V. Aslanyan[1,a], S. Taimourzadeh[2], L. Shi[2], Z. Lin[2], G. Dong[3], P. Puglia[4], M. Porkolab[1], R. Dumont[5], S.E. Sharapov[6], J. Mailloux[6], M. Tsalas[6], M. Maslov[6], A. Whitehead[6], R. Scannell[6], S. Gerasimov[6], S. Dorling[6], S. Dowson[6], H.K. Sheikh[6], T. Blackman[6], G. Jones[6], A. Goodyear[6], K.K. Kirov[6], P. Blanchard[4], A. Fasoli[4], D. Testa[4] and JET Contributors[b]

[1] MIT PSFC, 175 Albany Street, Cambridge, MA 02139, United States of America
[2] Department of Physics and Astronomy, University of California, Irvine, CA 92697, United States of America
[3] Princeton Plasma Physics Laboratory, Princeton University, Princeton, NJ 08543, United States of America
[4] Ecole Polytechnique Fédérale de Lausanne (EPFL), Swiss Plasma Center (SPC), CH-1015 Lausanne, Switzerland
[5] CEA, IRFM, F-13108 Saint-Paul-lez-Durance, France
[6] CCFE, Culham Science Centre, Abingdon, OX14 3DB, United Kingdom of Great Britain and Northern Ireland

E-mail: aslanyan@mit.edu

Received 24 May 2018, revised 9 November 2018
Accepted for publication 27 November 2018
Published 21 December 2018

Abstract

The gyrokinetic toroidal code (GTC) has been used to study toroidal Alfvén eigenmodes (TAEs) in high-performance plasmas. Experiments performed at the Joint European Torus (JET), where TAEs were driven by energetic particles arising from neutral beams, ion cyclotron resonant heating, and resonantly excited by dedicated external antennas, have been simulated. Modes driven by populations of energetic particles are observed, matching the TAE frequency seen with magnetic probes in JET experiments. A synthetic antenna, composed of one toroidal and two neighboring poloidal harmonics has been used to probe the modes' damping rates and quantify mechanisms for this damping in GTC simulations. This method was also applied to frequency and damping rate measurements of stable TAEs made by the Alfvén eigenmode active diagnostic in these discharges.

Keywords: energetic particle, Alfvén wave, toroidal Alfvén eigenmode

(Some figures may appear in colour only in the online journal)

[a] Author to whom any correspondence should be addressed.
[b] See the author list of [25].

1. Introduction

Toroidal Alfvén Eigenmodes (TAEs) are one of the most frequently observed [1, 2] examples of a class of electromagnetic instability driven by energetic particles in tokamaks and are of mounting concern for future experiments. A population of particles, resulting from wave and beam heating schemes and increasingly directly from fusion reactions, can destabilize TAEs leading to the expulsion of energetic particles and first wall damage [3, 4]. In this Article, we report the results of recent simulation efforts with the gyrokinetic toroidal code (GTC) [5] to determine the structure and stability of TAEs in recent JET discharges.

Spatial gradients of the densities and temperatures of energetic particles are a source of free energy contributing to the TAEs' linear growth rate γ_L, which is counteracted by damping from several mechanisms. Continuum damping in the TAE frequency gap, formed by the coupling of two adjacent poloidal harmonics, is typically insignificant. Electron and ion Landau damping typically form a significant contribution; radiative damping, whereby the TAEs couple to kinetic Alfvén waves and dissipate energy, can dominate over other damping mechanisms.

The conventional approach to numerical investigations of TAEs and their growth and damping rates is to compute the eigenmode structure and real frequency, often with an ideal-MHD code like MISHKA [6, 7], and perturbatively compute dissipative rates and the contributions of energetic particles [8]. The advantage of the gyrokinetic approach in this work is the self-consistent solution to the structure and drive/damping mechanisms, even in the presence of a significant population of energetic ('fast') ions. The simulations presented in this Article are a first step towards nonlinear simulations required for planned future DT experiments.

In order to explore and quantify the phenomenon of TAEs at JET since the installation of the fully-metal ITER-like wall, discharges have been tailored to their observation [9]. In particular, experiments with deuterium were undertaken with the aim of developing a scenario for clear observation of α-driven TAEs in future DT experiments. Discharges with relatively low densities, internal transport barriers and elevated q-profiles were performed to this end. Heating by $\gtrsim$5 MW of ion cyclotron resonant heating (ICRH) and $\gtrsim$25 MW of neutral beam (NBI) power was applied with various degrees of overlap. Consequently, TAEs were routinely destabilized during these experiments; a spectrogram of multiple unstable TAEs during application of ICRH is shown in figure 1.

During these discharges, the stable TAEs were probed by the newly upgraded Alfvén eigenmode active diagnostic (AEAD) [10, 11]. Two sets of antennas, located at toroidally opposite locations below the outboard midplane, apply a magnetic perturbation at ~10 cm from the last closed flux surface (LCFS). The antennas' frequency was continuously swept across the TAE gap in order to resonantly excite stable modes, as seen in the triangular waveform in figure 1. A magnetic probe measurement of a mode's response to this type of excitation is described by a transfer function, which allows the mode's frequency and damping rate in the absence of energetic particle drive to be determined. The AEAD can be phased to maximize the excitation spectrum at some toroidal mode number of interest exciting $\Delta n \sim \pm 10$ around this peak.

In this article, we will outline the theoretical basis, workflow and initial results of simulations of JET plasmas using GTC. In section 2, we review the formulation of GTC and the details of JET simulations. In section 3 we outline in detail the calculations of the spatial structure and growth rate of an unstable TAE (driven by energetic ions), and the contribution to the mode's damping by electron Landau, ion Landau and radiative damping. In section 4 we repeat this process for stable modes resonantly excited by external antennas.

2. Details of gyrokinetic simulations

The gyrokinetic toroidal code (GTC) [5] treats a population of bulk ions and a separate population of energetic ions with the δf particle-in-cell method (though a full-f method is also available). For a full description of the 5D system of equations solved by GTC, see [12–16]. The gyrokinetic equation for the distribution of species α (which can be used to index i.e. f for ions, electrons and 'fast' ions) is

$$\frac{\mathrm{d}}{\mathrm{d}t}f_\alpha(\mathbf{X},\mu,v_\parallel,t) \equiv \left[\frac{\partial}{\partial t} + \left(v_\parallel \frac{\mathbf{B}}{B_0} + \mathbf{v}_E + \mathbf{v}_\mathbf{d}\right)\cdot\nabla - \left(\frac{1}{m_\alpha}\frac{\mathbf{B}^*_\alpha}{B_0}\cdot(\mu\nabla B_0 + Z_\alpha\nabla\phi) + \frac{Z_\alpha}{m_\alpha c}\frac{\partial A_\parallel}{\partial t}\right)\frac{\partial}{\partial v_\parallel}\right] f_\alpha = 0, \tag{1}$$

where $\mathbf{X}$ is the gyrocenter position, μ the magnetic moment, the unperturbed magnetic field $\mathbf{B}_0 \equiv B_0\mathbf{b}_0$, and m_α, Z_α are the particle mass and charge respectively (q_e is the electronic charge). Here, $v_\parallel$ is the parallel velocity,

$$\mathbf{v}_E = c\frac{\mathbf{b}_0\times\nabla\phi}{B_0} \tag{2}$$

is the $E\times B$ drift velocity,

$$\mathbf{v}_d = \frac{1}{\Omega_\alpha}\left(v_\parallel^2\nabla\times\mathbf{b}_0 + \frac{\mu}{m_\alpha}\mathbf{b}_0\times\nabla B_0\right) \tag{3}$$

is the magnetic drift velocity with gyrofrequency Ω_α, and

$$\mathbf{B}^*_\alpha = \mathbf{B}_0 + \frac{B_0 v_\parallel}{\Omega_\alpha}\nabla\times\mathbf{b}_0 + \delta\mathbf{B}. \tag{4}$$

$\delta\mathbf{B} = \nabla\times A_\parallel\mathbf{b_0}$ is the perturbed magnetic field. The perturbed vector and electrostatic potentials are $A_\parallel$ and ϕ, respectively, and are gyroaveraged for ions and taken at the gyrocenter for electrons.

In this work, we split the distribution functions of ions into equilibrium and perturbed components $f_\alpha = f_{0\alpha} + \delta f_\alpha$, to solve

$$\frac{d(\delta f_\alpha/f_\alpha)}{\mathrm{d}t} = \left[\frac{\delta f_\alpha}{f_\alpha f_{0\alpha}} - \frac{1}{f_{0\alpha}}\right]\left[\left(v_\parallel\frac{\delta\mathbf{B}}{B_0} + \mathbf{v}_E\right)\cdot\nabla f_{0\alpha} - \frac{1}{m_\alpha}\left(\mu\frac{\delta\mathbf{B}}{B_0}\cdot\nabla B_0 + Z_\alpha\frac{\mathbf{B}^*_\alpha}{B_0}\cdot\nabla\phi + \frac{Z_\alpha}{c}\frac{\partial A_\parallel}{\partial t}\right)\frac{\partial f_{0\alpha}}{\partial v_\parallel}\right]. \tag{5}$$

The electrostatic potential can be found using gyrokinetic Poisson's equation [17],

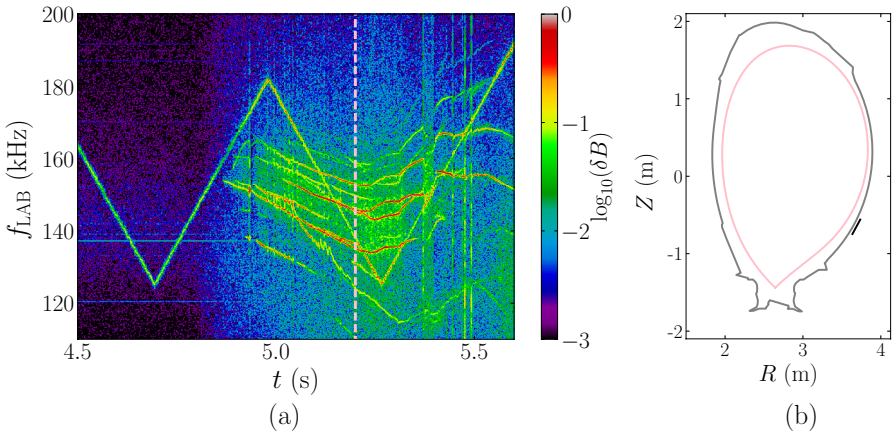

Figure 1. (*a*) Spectrogram of ICRH-driven TAEs in JPN #92416. GTC simulation time (5.2 s) is marked by pink dashed line. The triangular waveform is the frequency scan by the AEAD. (*b*) Corresponding shape of the LCFS from EFIT, relative to the limiters (grey) and AEAD antennas (black).

$$\frac{Z_i^2 n_i}{T_i}(\phi - \tilde{\phi}) = \sum Z_\alpha \delta n_\alpha. \tag{6}$$

The term $\phi - \tilde{\phi}$ on the left hand side represents the ion polarization density and $\tilde{\phi}$ is the double gyroaverage of ϕ [17]. The vector potential satisfies the gyrokinetic Ampère's law,

$$\nabla_\perp^2 A_\parallel = \frac{4\pi}{c}\sum Z_\alpha n_\alpha \delta u_{\parallel\alpha}. \tag{7}$$

The density and parallel velocity are defined as the fluid moments (gyroaveraged for ions) of the corresponding distribution functions,

$$\begin{aligned} \delta n_\alpha &= \int \mathrm{d}\mathbf{v}\delta f_\alpha, \\ n_\alpha \delta u_{\parallel\alpha} &= \int \mathrm{d}\mathbf{v} v_\parallel \delta f_\alpha. \end{aligned} \tag{8}$$

Equations (1)–(8) form a complete system when applying to thermal and fast ions as well as electrons. For reasons of computational efficiency of simulating Alfvén Eigenmodes where tearing parity is not important, the electrons are treated by a fluid-kinetic hybrid electron model [18]. Namely, the perturbed distribution function is $\delta f_e = \delta f_e^{(0)} + \delta h$, where $\delta f_e^{(0)}$ and δh are the adiabatic and nonadiabatic parts of the perturbed electron distribution, respectively, and $|\delta f_e^{(0)}| \gg |\delta h|$. The continuity equation is used for the perturbed electron density δn_e, to first order in the perturbation, becomes [12]

$$\begin{aligned} \frac{\partial \delta n_e}{\partial t} + B_0 \mathbf{b}_0 \cdot \nabla\left(\frac{n_0 \delta u_{\parallel e}}{B_0}\right) + B_0 \mathbf{v}_e \cdot \nabla\left(\frac{n_0}{B_0}\right) \\ - n_0(\mathbf{v}_* + \mathbf{v}_E)\cdot\frac{\nabla B_0}{B_0} = 0, \end{aligned} \tag{9}$$

where n_0 is the equilibrium density, $\delta u_{\parallel e}$ is the perturbed parallel electron fluid velocity and

$$\mathbf{v}_* = \frac{1}{n_0 m_e \Omega_e}\mathbf{b}_0 \times \nabla(\delta P_\parallel + \delta P_\perp), \tag{10}$$

$$\delta P_\parallel = \int \mathrm{d}\mathbf{v}\mu B_0 \delta f_e, \tag{11}$$

$$\delta P_\perp = \int \mathrm{d}\mathbf{v} m v_\parallel^2 \delta f_e. \tag{12}$$

To obtain an expression for $\delta f_e^{(0)}$, we expand equation (1) to first order in $\omega/k_\parallel v_\parallel$:

$$v_\parallel \mathbf{b}_0 \cdot \nabla \delta f_e^{(0)} = v_\parallel \left(\frac{f_0 q_e}{T_e}\mathbf{b}_0 \cdot \nabla \phi_{\rm eff} - \frac{\delta \mathbf{B}}{B_0}\cdot \nabla f_0|_{v_\perp}\right). \tag{13}$$

The notation $\nabla f|_{v_\perp}$ implies a derivative taken at $v_\perp = \text{const}$ instead of $\mu = \text{const}$. The effective potential represents the parallel electric field through $\delta E_\parallel = -\mathbf{b}_0 \cdot \nabla \phi_{\rm eff}$. The effective potential is, to lowest order,

$$\frac{q_e \phi_{\rm eff}^{(0)}}{T_e} = \frac{\delta n_e}{n_0} - \frac{\delta\psi}{n_0}\frac{\delta n_0}{\delta \psi_0} - \frac{\delta\alpha}{n_0}\frac{\delta n_0}{\delta \alpha_0}, \tag{14}$$

where $\delta\psi$ and $\delta\alpha$ are magnetic field line perturbations. We calculate the vector potential $\delta A_\parallel$ from the inductive potential $\phi_{\rm ind} = \phi_{\rm eff} - \delta\phi$ through

$$\frac{\partial \delta A_\parallel}{\partial t} = c\mathbf{b}_0 \cdot \nabla \phi_{\rm ind}, \tag{15}$$

which also provides the time derivative of $\delta A_\parallel$ used in equations (1) and (8). The parallel velocity $\delta u_{e\parallel}$ needed for equation (5) is calculated through Ampère's law, i.e. equation (7) is used to solve for $\delta u_{e\parallel}$ on the right hand side. Equations (1)–(15) form a complete system using fluid (adiabatic) electrons. These lowest order equations of the fluid-kinetic model can be used to remove the effects of kinetic electrons (electron Landau damping and trapped electrons).

The kinetic effects of electrons are treated in the higher order kinetic equations. Using equations (1) and (13), we calculate δh with,

$$\begin{aligned} \frac{d(\delta h_e/f_e)}{\mathrm{d}t} = \left[\frac{\delta h_e}{f_e} + \frac{\delta f_e^{(0)}}{f_{0e}} - 1\right]\left[\mathbf{v}_E \cdot \frac{\nabla f_{0e}|_{v_\perp}}{f_{0e}} + \frac{\partial}{\partial t}\frac{\delta f_e^{(0)}}{f_{0e}}\right. \\ + \mathbf{v}_d \cdot \nabla \frac{\delta f_e^{(0)}}{f_{0e}} - \frac{q_e}{T_e}\mathbf{v}_d \cdot \nabla\phi + c\frac{\mathbf{b}_0 \times \nabla\langle\phi\rangle}{B_0}\cdot\nabla\frac{\delta f_e^{(0)}}{f_{0e}} \\ \left. - \frac{q_e v_\parallel}{cT_e}\frac{\partial\langle A_\parallel\rangle}{\partial t}\right], \end{aligned} \tag{16}$$

where $\langle\rangle$ denotes flux-surface averaging such that $\phi = \langle\phi\rangle + \delta\phi$ and similarly for $A_\parallel$. Kinetic electron effects are calculated using the first order correction to the effective potential $\phi_{\rm eff} = \phi^{(0)}_{\rm eff} + \phi^{(1)}_{\rm eff}$, where $\phi^{(1)}_{\rm eff}$ is given by

$$\frac{q_e\phi^{(1)}_{\rm eff}}{T_e} = -\frac{\delta n^{(1)}_e}{n_e}, \delta n^{(1)}_e = \int {\rm d}\mathbf{v}\delta h_e. \tag{17}$$

All particle species in GTC are assumed to have their own, spatially-dependent Maxwellian distributions (wth the exception of energetic ions, see below). GTC uses a field-aligned mesh in Boozer coordinates, which is computed based on an EFIT [19] equilibrium reconstruction, that is mapped to Boozer coordinates by the ORBIT [20] code. GTC simulations reported in this paper use a fixed boundary condition: namely, all perturbed quantities are set to be zero at the inner and outer boundary flux surfaces.

The synthetic antenna imposes an electrostatic perturbation $\delta\phi_{\rm ant}$ (a perturbation of the parallel vector potential $\delta A_{\parallel{\rm ant}}$ is also available) consisting of a number of toroidal and poloidal spatial components and sinusoidal temporal oscillations at a user-defined frequency. For the purposes of this work, an antenna structure with a single n and two neighboring m, $m+1$ mode numbers of identical magnitude and an approximately Gaussian radial profile is chosen to closely resemble the destabilized TAE structure. These Gaussian radial profiles are imposed only in the plasma inside the simulation domain, i.e. no vacuum regions are simulated.

The flux surface dependent electron density and temperature was taken from JET's high resolution Thomson scattering and LIDAR diagnostics, which for $t = 5.2$ s in JPN #92416 is given by the points in figures 3(*a*) and (*b*). Data from this and adjacent time slices is smoothed into quasi-analytic, monotonic functions given by the solid lines in each panel in order to avoid any unphysically large spatial gradients. At the simulation times chosen for this work, the bulk ion temperature determined by spectroscopic measurements was relatively close to that of the electrons, namely $T_i \approx T_e$. The safety factor from the EFIT equilibrium reconstruction, used by GTC as outlined above, is given in figure 3(*c*).

3. Calculation of mode structure and damping rates

For each JET equilibrium used in GTC simulations (taken at the experimental times of interest), we calculate the structure of the Alfvén continuum using the ALCON [21] code, which includes acoustic effects. The $n = 5$ continuum in JPN #92416 at 5.2 s (pink line in figure 1) is shown in figure 4; note that the symbol ψ_p denotes the poloidal flux normalized to the edge value. This $n = 5$ mode was chosen for analysis as it is observed destabilized with an approximately constant amplitude for a significant length of time. The observed TAE, after adjusting for the Doppler shift due to plasma rotation, is within the predicted TAE gap.

A population of energetic ions (typically much smaller than the bulk ions) can be treated in GTC as either a Maxwellian where $f(v) \propto \exp(-m_\alpha v^2/2T_\alpha)$, as used in this work, or a beam slowing down distribution where $f(v) \sim v^{-3}$, isotropic in both cases. It is known that the non-equilibrium distributions produced by external heating methods are directional and may have a complicated functional form. However, for the present work we assume the that the destablizing effects of energetic ions are insensitive to the precise nature of the distribution function in line with other simulations. In order to simulate energetic particle drive, we must therefore define an effective 'fast' ion temperature T_f and density n_f. As direct measurements of these quantities are difficult to obtain, we smooth the density profile predicted by ICRH (and, optionally NBI) codes; this is then used to obtain an effective temperature through $E_f = \frac{3}{2}T_f n_f$, where E_f is the total intantaneous absorbed energy content of the energetic ions, also calculated by such codes. For the present case, we take a centrally peaked energetic particle population accelerated by ICRH, computed by the PION code [22], given in figure 3(*d*). Here, $T_f(\psi_p = 0) = 747$ keV, dropping to $T_f(\psi_p = 0.258) = 550$ keV at the peak of the mode of interest and with $n_f/n_e = 4.9\times10^{-3}$ at this flux surface. Note that once the n_e and n_f profiles are chosen as described above, the bulk ion density n_i is calculated from quasineutrality.

The mode of interest with $n = 5$ and two dominant poloidal harmonics $m = 11$ and $m = 12$ grows from random initial perturbations. The mode's frequency and growth rate can be determined after a length of simulation time, when the amplitude of the mode has grown sufficiently and the other harmonics are damped to low amplitudes. This growth of the electrostatic potential of the mode's $m = 12$ harmonic (for a simulation with kinetic electrons and gyrokinetic ions) is shown in figure 2(*a*) with an indicative exponential envelope. The spatial mode structure is shown in figure 2(*c*), with $f = 110$ kHz and a net growth rate of $\gamma/\omega = +1.38\%$ (by convention we explicitly specify positive γ for growth). We note that the frequency is within the TAE gap and closely matches the observed frequency, as shown in figure 4; the full width half-maximum (FWHM) of the flux surface averaged electrostatic perturbation is given by the horizontal bars for the energetic particle driven mode and antenna excitation as detailed below. To obtain the rate of electron Landau damping, we repeat the simulation with the fully adiabatic electron model; in this case the frequency and mode structure are both largely unchanged, but the increase in growth rate (now $\gamma/\omega = +1.47\%$) is attributable to the disappearance of kinetic electron effects. To transform from GTC simulations in the plasma frame to the laboratory, where $f_{\rm LAB} - f = nf_{\rm ROT}$, we assume that the frequency of unstable TAEs of neighboring toroidal numbers are approximately equal in the plasma frame as predicted by ideal MHD and therefore deduce the plasma rotation frequency $f_{\rm ROT}$. Note that TAE frequency could weakly depend on toroidal number n in the plasma frame due to pressure gradients of thermal plasmas, which contribute to both TAE real frequency and growth rate [16].

The response of a damped eigenmode in GTC to external excitation by an antenna with a driving angular frequency ω_d is similar to that of a damped driven harmonic oscillator (as is that of a physical antenna), producing a beat pattern and then tending to a saturated response after a number of cycles. The

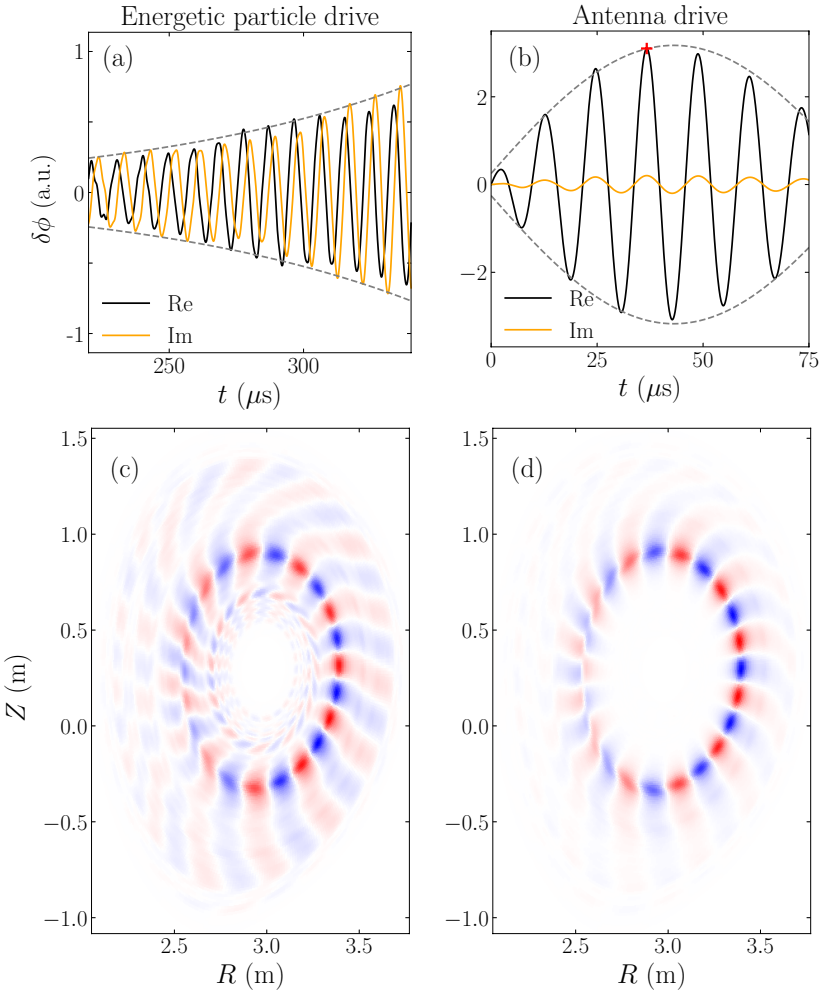

Figure 2. Time-dependent electrostatic potential perturbation (dark—imaginary and light—real components) of (*a*) energetic particle driven and (*b*) antenna driven TAE with $n = 5$. An indicative exponential and sinusoidal envelope is given for each respective plot by the grey dashed line. The red cross in (*b*) indicates the time when the peak amplitude is taken for the purposes of damping rate calculation (see below). The corresponding spatial mode structures are given by (*c*) and (*d*) respectively.

peak amplitude in this case is given by a Lorentzian distribution of the form

$$A(\omega_d) = \frac{A_0}{\sqrt{(\omega_d^2 - \omega^2)^2 + (2\gamma\omega_d)^2}}, \tag{18}$$

where the parameters to be fitted are the scale factor A_0, the real part of the angular frequency ω and the damping rate γ of the eigenmode. Note that this antenna drive is applied in the plasma frame, in the simulations. The sinusoidal beat frequency envelope appearing in present simulations is shown in figure 2(*b*). The peak is taken to be the first maximum, at a time indicated in this case by the red cross: in fact, the peak itself is taken from the modulus of the mode amplitude.

In order to quantify damping mechanisms other than electron Landau damping, we perform a simulation without the fast ions and apply the synthetic antenna at the same radial location as the energetic particle mode. Such a mode structure, for a simulation with fluid-kinetic electrons and gyrokinetic ions, is given in figure 2(*d*). Repeating the simulation for multiple drive frequencies allows a fit to determine the parameters in equation (18) to be performed, as shown in figure 5; the derived damping rate ($\gamma/\omega = -2.82\%$) in this case is due to both ion Landau and radiative damping. This procedure is repeated for the ideal MHD formulation of GTC [13], where ion Landau damping is not present ($\gamma/\omega = -1.18\%$). A heirarchy of mechanisms is obtained by taking the difference in the total drive or damping rates of simulations with different physics models to obtain a net rate, as summarized in table 1.

4. External antenna excitation

Six antennas of the AEAD were operated during these experiments, with groups of four and two at toroidally opposite locations, each producing a peak magnetic field of approximately 8×10^{-5} T at the LCFS. With the system's recent upgrade, each antenna is now driven by an individual amplifier, allowing arbitrary phase control between the antennas. The resonant excitation of marginally stable AE by such

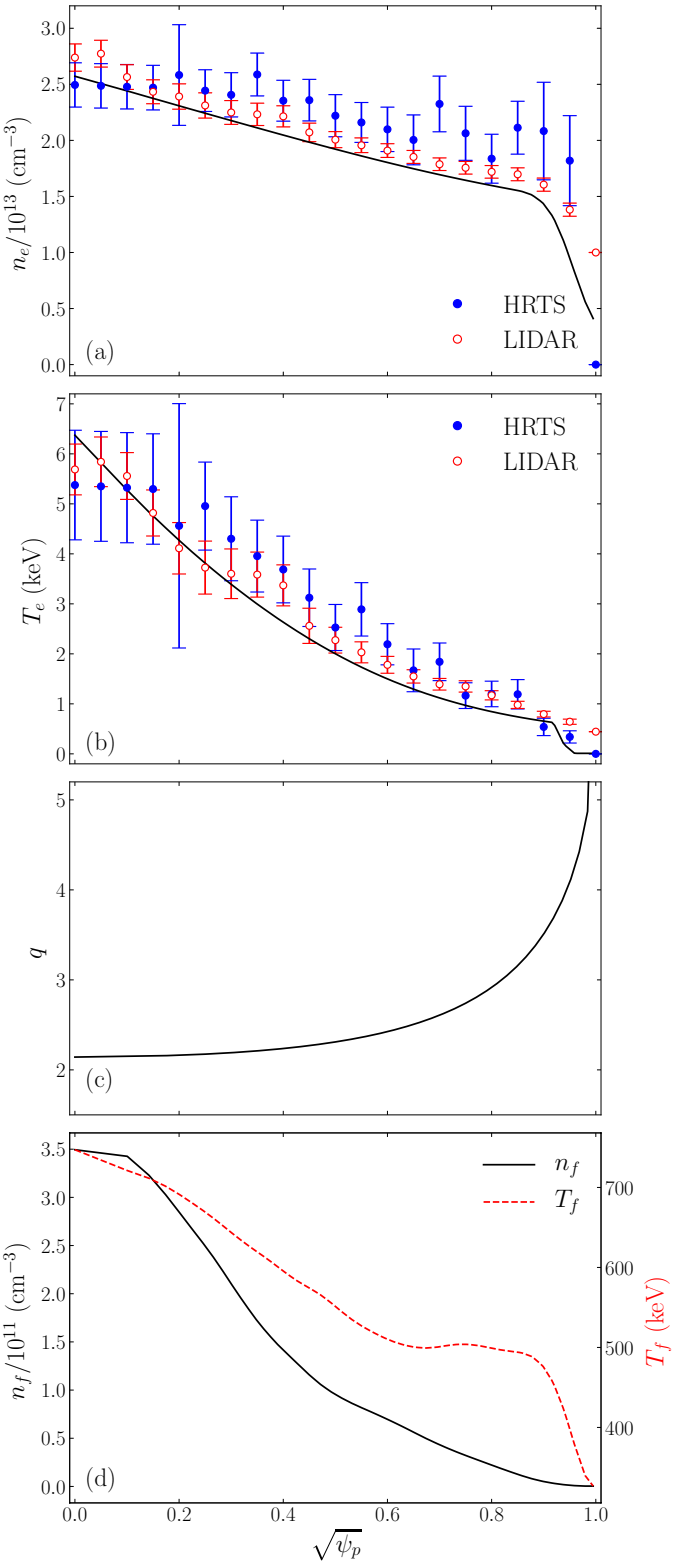

Figure 3. The electron (*a*) density and (*b*) temperature profiles (solid line) at 5.2 s in JPN #92416, compared to diagnostics. (*c*) Safety factor computed by `EFIT`. (*d*) Fast ion density (solid) and temperature (dashed), assumed to be isotropic, derived from ICRF simulations. Furthermore, for the bulk ions we have $T_i = T_e$ and n_i derived through quasineutrality.

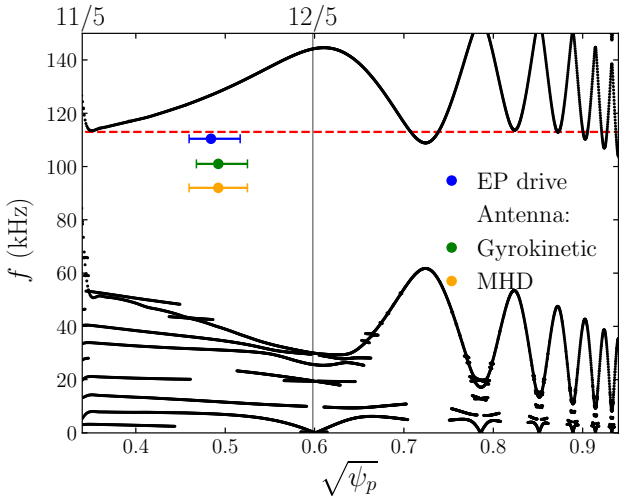

Figure 4. Alfvén continuum (black dotted lines) for $n = 5$ for the energetic particle simulation parameters (pink line in figure 1: 5.2 s in JPN #92416). The frequency and peak position of the modes are given by the colored points; the corresponding FWHM is given by the horizontal bars. The modes are driven by energetic particles, the synthetic antenna with gyrokinetic ions and with the reduced (MHD-like) model, as labelled. Note that the FWHM and frequency in the EP drive case is almost identical for both the kinetic and adiabatic electron case. The red dashed line represents the observed TAE plasma frame frequency. The $11/5$ and $12/5$ rational surfaces, which bracket the mode, are indicated.

magnetic perturbations is detected by a toroidal array of high-resolution magnetic probes. The probe signal is related to the driver input of frequency ω_d by a complex-valued transfer function [10]

$$H(\omega_d) = \frac{C\omega^2 + \mathrm{i}D\omega_d\omega}{\omega^2 - \omega_d^2 + 2\mathrm{i}|\gamma|\omega_d}, \tag{19}$$

where ω and γ are the mode's frequency and damping rate (with measurements in the laboratory frame), and C and D are amplitude parameters. The mode number can be identified from the phase differences between probes, provided that measurements can be obtained at a sufficiently large number of toroidal points.

Three measurements of TAEs made in two discharges suitable for analysis with GTC are shown in figure 6(*a*); table 2 contains their details and labels for reference. The derived values of the frequency and damping rate are obtained by fitting the transfer function of equation (19) to the appropriate signals as shown for one of the probes in case 2 in figure 6(*b*). The experiments discussed here were undertaken when the majority of the toroidal magnetic probes had become defective or miscalibrated prior to a major shutdown and refurbishment. This has led both to the large margin of error in the damping rate measurements and to difficulties in identifying the TAEs' toroidal mode number. We therefore perform the above analysis with the synthetic antenna in GTC—identifying the peak amplitude for different drive frequencies—for multiple mode numbers to identify a suitable candidate mode. Of these simulated candidates, the closest to the measured mode in both the frequency and damping rate can be matched to the experiment.

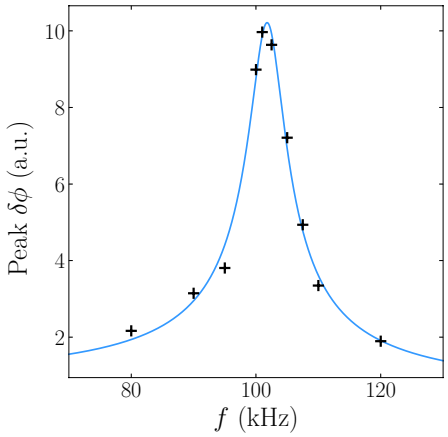

Figure 5. Spectral response to synthetic antenna excitation in GTC for a TAE with $n = 5$. Peak amplitudes as a function of frequency are given by crosses, the fit function with $f = 101$ kHz and $\gamma/\omega = -2.82\%$ by the solid line.

Table 1. Drive and damping mechanisms for the $n = 5$ TAE observed in JPN #92416 at 5.2 s. The total drive or damping rate, obtained directly from the corresponding simulation, is used to deduce net rate for each mechanism; the net rate is that due to the corresponding mechanism alone in the absence of the other mechanisms.

	Drive/Damping γ/ω	
Mechanism	Total (%)	Net (%)
Continuum	~ 0	~ 0
Radiative	-1.18	-1.18
Ion Landau	-2.82	-1.64
Energetic particle	$+1.47$	$+4.29$
Electron Landau	$+1.38$	-0.09

For the mode in case 2, the Alfvén continuum is plotted in figure 7. Note that the q profile has evolved significantly in time since the equilibrium profile in figure 3(*d*), with $q(0) < 1$ and consequently higher Alfvén frequency. We probe the TAE gap with a synthetic antenna with two neighboring poloidal harmonics; the driving signal is localized between the two corresponding rational surfaces to maximize the excitation. For example, when investigating a mode with $n = 5$, $m = 5, 6$, the radial peak of the synthetic antenna signal would be located between $q = 5/5$ and $q = 6/5$. For four prospective modes, the resulting frequencies, mode localization and damping rates are shown in figure 7. Based on this analysis, we see that the $n = 6$, $m = 5, 6$ mode located around $\psi_p = 0.12$ most closely fits the observed laboratory frame frequency and damping rate. ICRH was active at the time of the AEAD measurement, but the $n = 6$, $m = 5, 6$ mode occurs sufficiently far from the absorption layer at $\psi_p = 0.267$ [8] that the stability is not affected by fast ions in this case.

We have repeated this analysis for the modes in the other two cases, as summarized in figure 8. The experimental uncertainty in the frequency detected by the AEAD in the laboratory frame is negligible, because the antenna driving frequency is a well-defined function of time and varies relatively slowly during mode detection; for this reason, we omit the AEAD

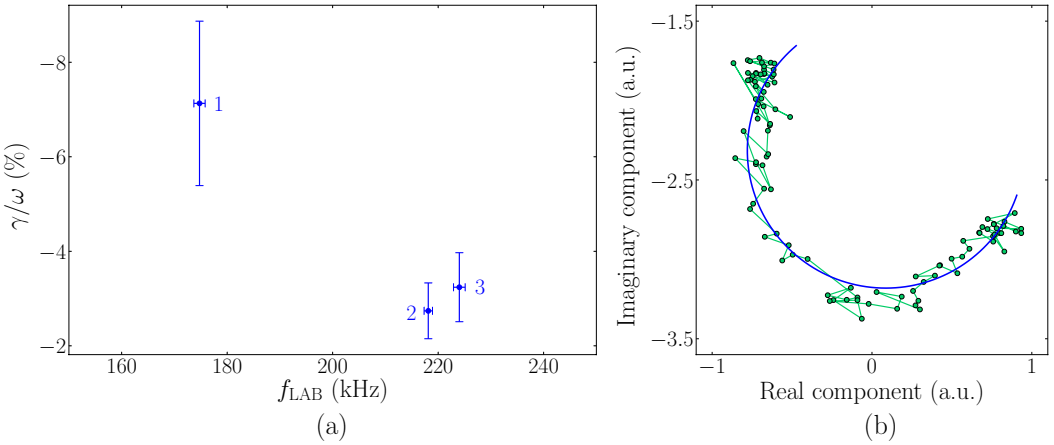

Figure 6. (*a*) The laboratory frame frequencies and damping rates of TAEs measured by the AEAD; the measurements are labelled by the cases given in table 2. (*b*) Magnetic probe datapoints (for case 2) acquired by the AEAD and the corresponding transfer function fit.

Table 2. Pulse numbers and times of the three AEAD measurement cases.

Case	JPN #	Time (s)
1	92416	4.9
2	92416	11.1
3	92060	7.7

frequency error bars from figure 8. Conversely, the uncertainty in the damping rate arises from fitting the transfer function to noisy signals from different magnetic probes and is consequently large. For case 1, a population of ICRH-accelerated ions taken from PION with $n_f(\psi_p = 0) = 3.6 \times 10^{11}$ cm^{-3} and $T_f(\psi_p = 0) = 461$ keV is used in the simulation. We find that a mode with $n = 9$, $m = 26, 27$ (the mde indicated for case 1 in figure 8) is damped sufficiently strongly even in the presence of the fast ions that it exceeds even the relatively strong damping seen in experiment. The calculated damping rate of the closest candidate mode with $n = 6$, $m = 11, 12$ in case 3 is a close match to experiment; no fast ions are modelled for this case as the measurement was made >500 ms (constituting multiple slowing down times) after ICRH had been switched off.

The uncertainty in matching the modes' frequency arises from the Doppler shift due to varying plasma rotation (which cannot be deduced in the absence of unstable modes). Direct spectroscopic measurements are available intermittently: only immediately following a 'notch' (rapid switch-off) in the neutral beam power, which allows the background signal to be subtracted. In figure 8 we transform the frequencies to the lab frame from the plasma frame as seen in GTC by the most probable rotation rate, based on an extrapolation from the closest spectroscopic measurement or the closest observable separation of other unstable modes. The lower error bound assumes zero rotation, while the upper error bound assumes that the rotation rate is exactly equal the closest observation. The measurement in case 2 is made much later than the end of neutral beam injection and therefore the plasma rotation is most likely negligible. Case 1 was taken as neutral beam injection was increasing rotation

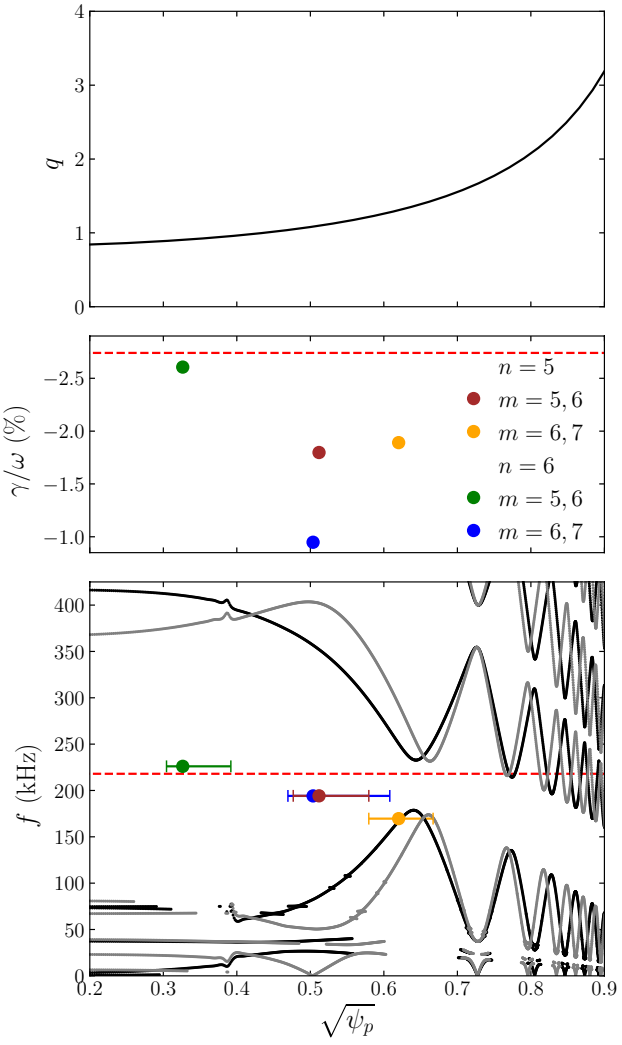

Figure 7. (Upper panel) The q profile at 11.1 s in JPN #92416. (Lower panel) Branches of the Alfvén continuum for $n = 5$ (black) and $n = 6$ (grey) showing the TAE gap. The frequencies and widths of modes probed by a synthetic antenna, with n and pairs of m as indicated, are shown relative to the continuum. (Middle panel) The corresponding damping rates. The red lines correspond to the laboratory frame frequency (see discussion below) and damping rate in the respective panels.

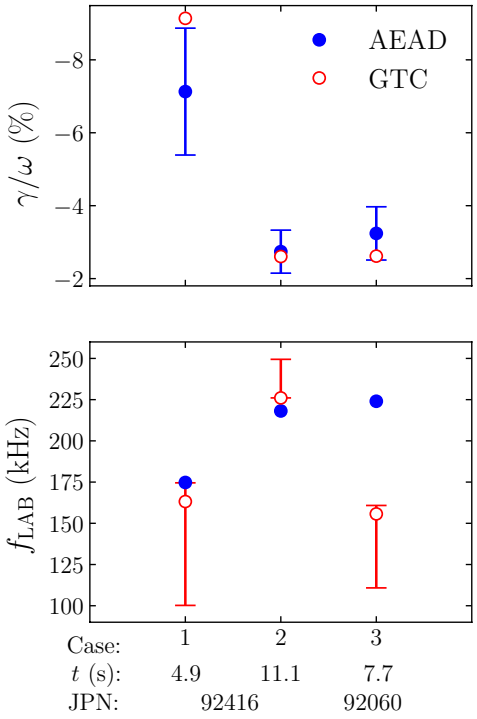

Figure 8. Comparison of the damping rate (top) and frequency (bottom) measured by the AEAD (solid circles) and simulated by GTC (empty circles). The uncertainties of the real frequency in the lab frame reflect the uncertainty in the measurement of the plasma rotation in the absence of concurrent rotation measurements.

and followed by a rotation measurement and *vice versa* for case 3. There is some discrepancy between the measured and simulated frequency in case 3, which may warrant further investigation.

5. Conclusion and outlook

We have presented the first simulations of TAEs in two JET pulses using GTC. The computations enable the modes' individual drive and damping mechanisms to be identified and quantified, from kinetic and non-perturbative models, which provide more physics insights than ideal MHD solvers. We have presented a heirarchical approach to the damping rate calculations, by applying different physics models, namely fully adiabatic and hybrid kinetic for electrons; ideal MHD and gyrokinetic for ions. A synthetic antenna is used to probe modes' frequencies and damping rate in the absence of drive by a population of energetic ions.

Simulations of a TAE driven unstable by ICRH-accelerated ions show good agreement with experiment. Its frequency has been matched to the that of the mode in the plasma frame as observed in the experiment and its damping mechanisms have been analyzed. Three measurements of stable TAEs made by the Alfvén eigenmode active diagnostic have been presented and analyzed with GTC. There are experimental challenges to be overcome in modelling these measurements: there is significant uncertainty in the mode number, stemming from a lack of magnetic probes (which have now been replaced and re-calibrated) and in the Doppler shift from the laboratory to the plasma frame, stemming from a lack of spectroscopic data. Nevertheless, the AEAD measurements are in reasonable agreement with the GTC simulations. We plan to use GTC to study lower frequency AEs on JET (in similar fashion to other machines [23, 24]) excited by energetic particles and the AEAD, and all AEs in the presence of α particles during the upcoming JET DT campaign.

Acknowledgments

This work has been part-funded by the RCUK Energy Programme [grant number EP/P012450/1]. Support for the MIT group was provided by the US DOE under Grant Number DE-FG02-99ER54563, and by SciDAC ISEP Center. This work used resources of the Oak Ridge Leadership Computing Facility at the Oak Ridge National Laboratory (DOE Contract No. DE-AC05-00OR22725) and the National Energy Research Scientific Computing Center (DOE Contract No. DE-AC02-05CH11231). This work has been carried out within the framework of the EUROfusion Consortium and has received funding from the Euratom research and training programme 2014–2018 under grant agreement No 633053. The views and opinions expressed herein do not necessarily reflect those of the European Commission.

References

[1] Wong K.-L. 1999 *Plasma Phys. Control. Fusion* **41** R1
[2] Heidbrink W.W. 2008 *Phys. Plasmas* **15** 055501
[3] ITER Physics Expert Group on Energetic Particles, Heating and Current Drive and ITER Physics Basis Editors 1999 *Nucl. Fusion* **39** 2471
[4] Duong H.H., Heidbrink W.W., Strait E.J., Petrie T.W., Lee R., Moyer R.A. and Watkins J.G. 1993 *Nucl. Fusion* **33** 749
[5] Lin Z., Hahm T.S., Lee W.W., Tang W.M. and White R.B. 1998 *Science* **281** 1835
[6] Mikhailovskii A.B., Huysmans G.T.A., Sharapov S.E. and Kerner W. 1997 *Plasma Phys. Rep.* **23** 844
[7] Huysmans G.T.A., Hender T. and Alper B. 1998 *Nucl. Fusion* **38** 179
[8] Nabais F. *et al* 2018 *Nucl. Fusion* **58** 082007
[9] Dumont R. *et al* 2018 *Nucl. Fusion* **58** 082005
[10] Fasoli A. *et al* 1995 *Phys. Rev. Lett.* **75** 645
[11] Puglia P. *et al* (JET Contributors) 2016 *Nucl. Fusion* **56** 112020
[12] Holod I., Zhang W.L., Xiao Y. and Lin Z. 2009 *Phys. Plasmas* **16** 122307
[13] Deng W., Lin Z. and Holod I. 2012 *Nucl. Fusion* **52** 023005
[14] Wang Z., Lin Z., Deng W., Holod I., Heidbrink W.W., Xiao Y., Zhang H., Zhang W. and Van Zeeland M. 2015 *Phys. Plasmas* **22** 022509
[15] Zhang W., Holod I., Lin Z. and Xiao Y. 2012 *Phys. Plasmas* **19** 022507
[16] Wang Z., Lin Z., Holod I., Heidbrink W.W., Tobias B., Van Zeeland M. and Austin M.E. 2013 *Phys. Rev. Lett.* **111** 145003

[17] Lee W.W. 1987 *J. Comput. Phys.* **72** 243
[18] Lin Z. and Chen L. 2001 *Phys. Plasmas* **8** 1447
[19] Lao L.L., St John H., Stambaugh R.D., Kellman A.G. and Pfeiffer W. 1985 *Nucl. Fusion* **25** 1611
[20] White R.B. and Chance M.S. 1984 *Phys. Fluids* **27** 2455
[21] Deng W., Lin Z., Holod I., Wang Z., Xiao Y. and Zhang H. 2012 *Nucl. Fusion* **52** 043006
[22] Eriksson L.-G., Hellsten T. and Willén U. 1993 *Nucl. Fusion* **33** 1037
[23] Zhang H.S., Lin Z., Holod I., Wang X., Xiao Y. and Zhang W.L. 2010 *Phys. Plasmas* **17** 112505
[24] Liu Y., Lin Z., Zhang H. and Zhang W. 2017 *Nucl. Fusion* **57** 114001
[25] Litaudon X. *et al* 2017 *Nucl. Fusion* **57** 102001